

Investigation and Optimization of Neon  
Soft X-ray of the INTI Plasma Focus at 12 kV

by

Federico Jr Apilado Roy



being a thesis submitted to  
INTI International University  
in candidature for the degree of  
Doctor of Philosophy

Centre for Plasma Research  
INTI International University  
2015



INTI  
International University  
LAUREATE INTERNATIONAL UNIVERSITIES

POSTGRADUATE PROGRAMME  
CERTIFICATION OF DOCTORAL THESIS

Author's Full Name	: <u>Federico Jr. Apilado Roy</u>
Student I.D	: <u>I11008931</u>
Thesis Title	: <u>Investigation and Optimization of Neon Soft X-Ray of the INTI Plasma Focus at 12KV</u>
Academic Session	: <u>May 2012 – May 2015</u>
With regard to Clause 4.2 of the INTI Student Intellectual Property Policy (Supplementary), the thesis is the student's property. Thereby declare this thesis as:	
CONFIDENTIAL	
<input type="checkbox"/>	Consisting of classified information under the OFFICIAL SECRETS ACT 1972.
RESTRICTED	
<input type="checkbox"/>	Consisting of RESTRICTED information which has been determined by the organisation/body where the research was conducted.
OPEN ACCESS/NON-RESTRICTED	
<input checked="" type="checkbox"/>	I allow this thesis to be published through open access, full text or copied for study, learning and research purposes only.
For the Open Access/Non-Restricted category, I allow this (Master's/Doctoral) thesis to be kept in the INTI International University (INTI) Library with the following usage conditions:	
1. INTI Library has the right to reproduce the thesis for study, learning and research purposes only.	
2. INTI Library is allowed to make one (1) copy of this thesis for exchange purpose among higher education institutions and any government body/agency, subject to terms and conditions.	
VERIFIED BY:	
	
STUDENT SIGNATURE	SUPERVISOR'S SIGNATURE
<u>E017176945</u>	<u>Professor Dr. Saw Sor Heoh</u>
(IDENTITY CARD/PASSPORT NO.)	DIRECTOR
Date: <u>16/4/2015</u>	SUPERVISOR'S NAME
	Centre for Plasma Research
	INTI International University
	Date: <u>17/4/2015</u>

### **COPYRIGHT**

The copyright of this thesis belongs to the author under the terms of the Copyright Act 1987 as qualified by Section 4 of INTI International University Intellectual Property Policy. Due acknowledgement shall always be made of the use of any material contained in, or derived from, this thesis.

© Federico Jr Apilado Roy, 2015  
All Rights reserved

### **DECLARATION**

I hereby declare that the work has been done by myself and no portion of the work contained in this thesis has been submitted in support of any application for any other degree or qualification of this or any other university or institute of learning.



---

**Federico Jr Apilado Roy**

## **ACKNOWLEDGEMENTS**

First and foremost the author gives glory to God who has given all His provisions and sustenance in the completion of this piece of work. Without His sovereign will, wisdom and guidance, this work is never accomplished.

Secondly, I am sincerely thankful to INTI International University for the scholarship and research grants INT CPR-03-08-2012 and FRGS/2/2013/SG02/INTI/01/1 that were used in the completion of the experimental work. In addition, I am also grateful to the Centre for Plasma Research for the laboratory facilities and Nanyang Technological University Singapore for the gift of 3kJ Plasma Focus Machine to INTI IU.

Thirdly, I am indebtedly appreciating the supervision of Prof. Saw Sor Heoh. In addition the help and support of Prof. Lee Sing is deeply appreciated. They have guided me in my journey in both the numerical and experimental aspect of this thesis. I have learnt a lot from them.

Lastly, I am blessed with the support of my wife Gloria Villena Roy. Her words of encouragements and love gave me the drive to go through this study.

I give back the glory to God for all the things that He has done.

## ABSTRACT

This thesis describes the theoretical and experimental investigations of the x-ray (specifically neon soft x-ray) properties and the plasma dynamics of the INTI Plasma Focus. The purpose of the research is two-fold, firstly to optimize the neon SXR yield of the INTI Plasma Focus (3 kJ, Mather type) machine; and secondly to investigate the correlation of the characteristic neon SXR signal pulse with the plasma focus dynamics.

The optimization of the SXR yield involved three steps. Firstly the optimization was carried out numerically using the 6 phase Lee Model Code (version RADPFV6.1b). The numerical experiments were accomplished at 12 kV to determine the optimum configuration for the electrodes using the INTI PF machine. The model parameters were determined and retained as  $f_m = 0.05$ ,  $f_c = 0.7$ ,  $f_{mr} = 0.2$  and  $f_{cr} = 0.8$ . The pressure (P), anode length (z), and anode radius (a) were parametrically varied while the value of cathode radius (b) was fixed at 3.2 cm. Secondly, the optimization experiments carried out at Centre for Plasma Research, INTI International University were guided by the numerical experiments with an optimized anode ('a' = 1.2 cm and z = 7.3 cm) designed as a screw-on type that retained the original radius until it just emerged out of the insulator sleeve. Thirdly, enhancement of yield was attempted by doping neon with krypton (Ne 97.5% + Kr 2.5%, Ne 95% + Kr 5%, Ne 90% + Kr 10% and Ne 80% + Kr 20%). Series of experiments using the original anode ('a' = 0.95 cm and z = 16 cm) were performed in the laboratory at 12 kV and operating neon gas pressure of 2.0 Torr. These experimental results were verified using the Lee Model code by adjusting the pressure for each admixture. The adjustments considered volumetric proportions of neon taking into account the difference in atomic weights (Ne-20 and Kr-84).

Finally, the correlation of characteristic neon SXR pulse with the plasma focus dynamics was investigated using a) the original anode of 16 cm length and 0.95 cm radius in neon, b) the optimized anode of 7.3 cm length and 1.2 cm radius in neon and c) the different Ne-Kr admixtures. Using the Lee Model code, an excel template was developed to plot the SXR pulse with the fitted measured and computed current traces. The template also shows different time markers such as the radial phase, the

## TABLE OF CONTENTS

	Page
COPYRIGHT	ii
DECLARATION	iii
ACKNOWLEDGEMENTS	iv
ABSTRACT	v
TABLE OF CONTENTS	vii
LIST OF TABLES	xi
LIST OF FIGURES	xiii
 CHAPTER 1 INTRODUCTION	
1.1 Background	1
1.2 Problem statement	5
1.3 Objectives of research	6
1.4 Literature review	7
1.4.1 Classification of x-ray sources	7
1.4.2 Development of plasma focus x-ray source	7
1.4.3 Research on SXR in plasma focus devices	9
1.4.4 High inductance and low inductance Mather type plasma focus machines	15
1.5 Measurement and monitoring of Ne SXR yield in plasma focus machine	15
1.6 Introducing our INTI PF	16
1.7 The INTI PF	18
1.8 Organization of thesis	21
 CHAPTER 2 DYNAMIC PROCESSES AND THE LEE MODEL OF THE RADIATIVE PLASMA FOCUS	
2.1 Introduction	22
2.2 The dynamics and phases occurring in the plasma focus	22



	Page
2.2.1 The breakdown phase	22
2.2.2 The axial acceleration phase	24
2.2.3 The radial phase	26
2.2.3.1 The radial inward shock phase	26
2.2.3.2 The reflected shock (RS) phase	27
2.2.3.3 The slow compression (Pinch Phase)	28
2.2.3.4 The unstable phase	29
2.2.3.5 The decay phase	30
2.3 Equations governing the axial phase	31
2.3.1 Snow plow equation of motion of axial phase	31
2.3.2 Circuit equation of axial phase	32
2.3.3 Related physical quantities	33
2.4 The radial inward shock phase	34
2.4.1 Speed of shock front	35
2.4.2 Speed of magnetic piston	36
2.4.3 Axial elongation speed of plasma slug	38
2.5 The radial reflected shock phase	38
2.5.1 The speed of reflected shock	38
2.5.2 The speed of magnetic piston	39
2.5.3 The circuit equation	39
2.6 The slow compression phase	40
2.6.1 The equation of motion (piston equation)	40
2.6.2 Axial elongation of the speed of plasma column	40
2.6.3 The circuit equation	41
2.6.4 The term $dQ/dt$ in Equation 2.37	41
2.7 Expanded column axial phase	41

### CHAPTER 3 CHARACTERISTICS OF SXR FROM PLASMA FOCUS

3.1 Introduction	42
3.2 Simplified plasma equilibrium model for plasma focus	42



		Page
3.2.1	General considerations of plasma equilibrium model	42
3.2.2	Corona model	43
3.2.3	Calculate ionization states	44
3.3	Calculation for neon plasmas using corona model	45
3.3.1	Equilibrium properties	45
3.3.2	X-ray power density from plasmas	48
3.3.3	X-ray emission intensities from neon plasma	51
3.3.4	Optimized conditions for x-ray radiative neon plasmas	55

#### CHAPTER 4 EXPERIMENTAL SET UP AND METHODOLOGY

4.1	Introduction	58
4.2	The plasma focus machine: INTI PF	58
4.3	Description of the INTI PF	59
4.4	Measurement of Ne SXR yield	60
4.4.1	The experiment	60
4.4.2	Estimation of Ne SXR yield by pin detector	61
4.4.3	The method for correlation of modeled dynamics with measured Ne-SXR time profiles	64
4.5	General procedures in the usage of the template to correlate the measured Ne SXR pulse with the computed plasma focus dynamics	67
4.6	Specific procedures in the usage of the template to correlate the Ne SXR measurements with plasma focus dynamics	70
4.7	Description of the template	70
4.8	Processing of data	71
4.9	Pre-fitting procedures	75
4.10	Fitting procedures	76
4.11	Numerical optimization of Ne SXR yield at 12 kV	79

	Page
CHAPTER 5 RESULTS AND FINDINGS	
5.1 Introduction	80
5.2 Results of the investigation of Ne SXR yield using the original anode	80
5.2.1 Comparison of measured with computed Ne SXR yields of INTI PF	81
5.2.2 Correlation of measured Ne SXR pulse with computed plasma focus dynamics	85
5.2.3 Experiment on Ne SXR yield from neon gas	87
5.2.4 Experiment on Ne SXR yield from Ne-Kr admixtures	110
5.3 The new anode designed to increase Ne SXR yield of INTI PF machine	137
5.3.1 Optimization of Ne SXR yield for the UNU/ICTP PFF	137
5.3.2 Optimization of Ne SXR yield for the INTI PF	139
5.3.3 Design of the anode for optimized Ne SXR yield	145
5.4 Comparison of measured and computed Ne SXR yields of INTI PF machine with new anode ( $a'=1.2$ cm and $z_0 = 7.3$ cm)	148
5.5 Correlation of the measured Ne SXR pulse and computed plasma focus dynamics for the optimized new anode	149
CHAPTER 6 CONCLUSIONS AND RECOMMENDATIONS	176
APPENDIX	179
REFERENCES	182
LIST OF PUBLICATIONS	188

## LIST OF TABLES

	Page
CHAPTER 3	
3.1 Optimization conditions for x-ray radiative Ne plasma	57
CHAPTER 4	
4.1 Operating parameters of the INTI PF	72
CHAPTER 5	
5.1 The breakdown of the 42 shots fired at 12 kV for Pure Ne	81
5.2 Computed plasma pinch parameters (using model parameters $f_m = 0.03$ ; $f_c = 0.7$ ; $f_{mr} = 0.2$ ; $f_{cr} = 0.7$ ) against P for INTI PF machine ( $L_0 = 110$ nH, $C_0 = 30\mu\text{F}$ , and $\text{RESF} = 0.2$ ), operating at 12 KV with the original anode ('a' = 0.95 cm and $z_0 = 16$ cm)	83
5.3 Average measured and computed (using fitted model parameters for each N type shot) Ne SXR versus P for standard INTI PF	84
5.4 Quantifying the correlation of measured Ne SXR pulse with computed (using fitted model parameters) plasma focus dynamics for N type shots	107
5.5 Description of each fitted shot in pure Ne	109
5.6 The breakdown of the 41 shots fired at 12 kV for Ne-Kr admixtures	110
5.7 Quantifying the correlation of measured Ne SXR pulse (Ne 97.5% + Kr 2.5%) with computed (using fitted model parameters) plasma focus dynamics for N type shots	116
5.8 Description of each fitted shot in Ne 97.5% + Kr 2.5% admixtures	117
5.9 Quantifying the correlation of measured Ne SXR pulse (Ne 95% + Kr 5%) with computed (using fitted model parameters) plasma focus dynamics for N type shots	122

	Page
5.10 Description of each fitted shot in Ne 95% + Kr 5% admixtures	123
5.11 Quantifying the correlation of measured Ne SXR pulse (Ne 90% + Kr 10%) with computed (using fitted model parameters) plasma focus dynamics for N type shot	128
5.12 Description of each shot in Ne 90% + Kr 10% admixtures	129
5.13 Quantifying the correlation of measured Ne SXR pulse (Ne 80% + Kr 20%) with computed (using fitted model parameters) plasma focus dynamics for N type shots	134
5.14 Description of each shot in Ne 80% + Kr 20% admixtures	135
5.15 Percentage of N and NN type for Ne-Kr admixtures	136
5.16 Numerical Ne SXR yields against P for the INTI PF at 12 KV with $L_0 = 110$ nH, $C_0 = 30\mu\text{F}$ , and $\text{RESF} = 0.2$ , $b = 3.2$ cm 'a' = 0.95 cm and $z_0 = 16$ cm, $f_m = 0.05$ , $f_c = 0.7$ , $f_{mr} = 0.2$ , $f_{cr} = 0.8$	140
5.17 Optimum combinations of $z_0$ and P obtained from numerical experiments carried out for INTI PF machine	141
5.18 Number of shots and operating pressures	148
5.19 Quantifying the correlation of measured Ne SXR pulse with computed plasma focus dynamics (using fitted model parameters) for N type shots with the new anode	169
5.20 Description of each fitted shot of the new anode	171
5.21 Percentage of N and NN type of the new anode ('a' = 1.2 cm and $z_0 = 7.3$ cm)	172
APPENDIX	
A-1 Basic parameters of neon gas	179
A-2 X-ray emission spectrum of highly ionized neon plasma	180

CHAPTER 3	Page
3.1 Neon ion fractions at different temperature. $N_i$ is the total ion (atom) number, $N_z$ is the $z_{th}$ ionized ion number (calculated by corona model)	45
3.2 Effective ionization number $Z_{eff}$ of Ne ions	47
3.3 Graph of ionization fraction against temperature for Krypton	47
3.4 Graph of effective charge against temperature for Krypton	48
3.5 Calculated emission intensities of Ne Ly $\alpha$ (1s-2p), Ly $\beta$ (1s-3p), He $\alpha$ (1s <sup>2</sup> -1s2p), and He $\beta$ (1s <sup>2</sup> -1s3p) lines. The dot lines are the fractions of H-like and He-like Ne ions. (based on corona model)	53
3.6 Calculated total continua emission of the Ne <sup>10+</sup> , Ne <sup>9+</sup> and Ne <sup>8+</sup> ions. The dot lines are the fractions of H-like and He-like Ne ions. $P_{bremS}$ and $P_{recS}$ are bremsstrahlung and recombination continua respectively	54
3.7 X-ray (Ly $\alpha$ + He $\alpha$ ) intensities	55
3.8 Ionization and thermal energies required for heating corona Ne and Kr plasmas	56
CHAPTER 4	
4.1 Block diagram of INTI PF: PFT plasma focus tube, GS gas supplier, PS power supply, C capacitor, SG spark gap, TC triggering circuit, DSO storage oscilloscope, and RP rotary pump, D voltage divider, RC rogowski coil.	59
4.2 Circuit for the swinging-spark gap and focus tube	59
4.3(a) A schematic of the pin-diode x-ray spectrometer side view	61
4.3(b) A schematic of the pin-diode x-ray spectrometer front view	61
4.4 Signal of XR1 (ch1) and XR2 (ch2) from the oscilloscope	62
4.5 The sensitivity of the two channels 1 and 2	62
4.6 Graph of $Y_{sxr}$ versus time, expanded from 3.12 $\mu$ s to 3.5 $\mu$ s	64



	Page
4.7	Illustrating 5 points fitting procedure where (a) is the time to peak current and (b) is start of current dip 65
4.8	A well fitted measured and computed current trace showing three Regions AR1, AR2 and AR3 66
4.9	Correlation of Ne SXR with measured and computed current traces 66
4.10(a)	Fitting procedures for axial and radial phase 68
4.10(b)	Fitting procedures for anomalous resistance phase 69
4.11(a)	The sheet 1 of the 6 phase Lee Model Code 70
4.11(b)	The sheet 2 of the 6 phase Lee Model Code 70
4.12	The sheet 3 of the 6 phase Lee Model Code 71
4.13	Details of sheet 1 of the 6 phase Lee Model Code 72
4.14	A typical set of graphs for the Lee Model Code 74
4.15	Measured and computed current trace with different time shift with other signals omitted to show current traces only. (pink trace is computed current, blue trace is measured current) 75
4.16	Measured and computed current trace with time shift corrected (pink trace is computed current, blue trace is measured current) 75
4.17	Measured and computed current trace with current amplitude scaling factor applied (pink trace is computed current, blue trace is measured current) 76
4.18	A well fitted measured and computed current trace ( pink trace is computed current, blue trace is measured current) 77
4.19	Expanded view of the measured and computed current trace from 3.4 $\mu$ s to 3.9 $\mu$ s 78

## CHAPTER 5

5.1	Measured and computed Ne SXR yield of the original anode ('a'= 0.95 cm, $z_0$ =16 cm) against gas pressures 84
5.2	Fitted measured and computed current waveforms at P = 2.0 Torr Ne at 12 kV 85

	Page
5.3	Correlating the measured characteristic He-like and H-like Ne SXR pulse (difference pulse of XR1 (Channel 1 signal) subtract XR2 (Channel 2 signal)) with the computed pinch phase. 86
5.4	Correlation of measured Ne SXR pulse to the computed reflected shock and the pinch phases of S1, S2, S3, S4 and S7 (all at 1.0 Torr) 89
5.5	Correlation of measured Ne SXR pulse to the computed reflected shock and pinch phases of S8, S9, S10, S11 and S12 (all at 1.5 Torr). 91
5.6	Correlation of measured Ne SXR pulse to the computed reflected shock phases of S13, S14, S15, S16 and S17 (all at 2.0 Torr). 93
5.7	Correlation of measured Ne SXR pulse to the computed reflected shock and pinch phases of S18, S19, S20, S21 and S22 (all at 2.5 Torr). 95
5.8	Correlation of measured Ne SXR pulse to the computed reflected shock and pinch phases of S23, S24, S25, S26 and S27 (all at 3.0 Torr). 98
5.9	Correlation of measured Ne SXR pulse to the computed reflected shock and pinch phases of S28, S29, S30, S31 and S32 (all at 3.5 Torr). 100
5.10	Correlation of measured Ne SXR pulse to the computed reflected shock and pinch phases of S33, S34, S35, S36 and S37 (all at 4.0 Torr). 102
5.11	Correlation of measured Ne SXR pulse to the computed reflected shock phase and the pinch phase of S39, S40, S41, and S42 (all at 4.5 Torr). 104
5.12	N and NN type with measured and computed Ne SXR yields against pressure for original anode ( $a' = 0.95$ cm, $z_0 = 16$ cm) 106



	Page
5.13 Correlation of Ne 97.5% + Kr 2.5% (S7-S17) measured Ne SXR pulse with the computed reflected shock and pinch phases.	115
5.14 Correlation of Ne 95% + Kr 5% (S18-S27) measured Ne SXR pulse with the computed reflected shock and pinch phases.	121
5.15 Correlation of Ne 90% + Kr 10% (S28-S37) measured Ne SXR pulse with the computed reflected shock and pinch phases.	127
5.16 Correlation of Ne 80% + Kr 20% (S38-S47) measured Ne SXR pulse with the computed reflected shock and pinch phases.	133
5.17 Numerical Ne SXR versus P for the UNU ICTP PFF with $L_0=110\text{nH}$ , $C_0=30\mu\text{F}$ , and $\text{RESF}=0.2$ , $b=3.2\text{ cm}$ , ' $a$ ' = 0.95 cm and $z_0 = 16\text{ cm}$ , operated at 14kV in Ne, with fitted model parameters $f_m=0.05$ , $f_c=0.7$ , $f_{mr}=0.2$ , and $f_{cr}=0.8$ .	138
5.18 Numerical Ne SXR versus P for the UNU ICTP PFF with $L_0=110\text{nH}$ , $C_0=30\mu\text{F}$ , and $\text{RESF}=0.2$ , $b=3.2\text{ cm}$ , ' $a$ ' = 1.2 cm and $z_0 = 7\text{ cm}$ , operated at 14kV in Ne, with fitted model parameters $f_m=0.05$ , $f_c=0.7$ , $f_{mr}=0.2$ , and $f_{cr}=0.8$ .	139
5.19 Computed Ne SXR against P for the INTI PF with $L_0=110\text{nH}$ , $C_0=30\mu\text{F}$ , and $\text{RESF}=0.2$ , $b=3.2\text{ cm}$ , ' $a$ ' = 0.95 cm and $z_0 = 16\text{ cm}$ , operated at 12kV Ne, with fitted model parameters $f_m=0.05$ , $f_c=0.7$ , $f_{mr}=0.2$ , and $f_{cr}=0.8$ .	140
5.20 Optimum Ne SXR yields at different pressures with different combination of anode radius and anode length.	142
5.21 Optimum Ne SXR yield at fixed anode length $z_0=7\text{ cm}$ and $P=1.6\text{ Torr}$ while anode radius is varied.	143
5.22 Optimum Ne SXR yield at fixed anode length $z_0 = 7\text{ cm}$ and anode radius ' $a$ ' = 1.407 cm while pressure P is varied.	143
5.23 Optimum Ne SXR yield at fixed anode radius ' $a$ ' = 1.2 cm while length $z_0$ and P is varied.	144
5.24 Results from numerical experiments comparing the Ne SXR yields of the original anode and the new anode.	144
5.25 Screwed-on anode for the INTI PF, optimized for Ne SXR yield	146

	Page
5.26	The INTI PF anodes (a) - the original ( $a' = 0.95$ cm and $z_0 = 16$ cm) and (b) the new screw-on anode ( $a' = 1.2$ cm and $z_0 = 7.3$ cm)
	147
5.27	The optimized anode and cathode rods of INTI PF
	147
5.28	Correlation of measured Ne SXR pulse with the computed reflected shock and pinch phases of the new anode for S3-S6, S9 and S11-S18 (all at 3.0 Torr).
	152
5.29	Correlation of measured Ne SXR pulse with the computed reflected shock and pinch phases of the new anode for S15 to S13 (all at 4.0 Torr).
	154
5.30	Correlation of measured Ne SXR pulse with the computed reflected shock and pinch phases of the new anode for S23-S25, S27-S28 and S31-S33 and S36-S37 (all at 5.0 Torr).
	158
5.31	Correlation of measured Ne SXR pulse with the computed reflected shock and pinch phases of the new anode for S39-S41, S43-S44, S46, S48 and S50-S53 (all at 6.0 Torr).
	162
5.32	Correlation of measured Ne SXR pulse the computed reflected shock phase and pinch phases of the new anode for S57 to S64 (all at 7.0 Torr)
	165
5.33	Correlation of measured Ne SXR pulse with the computed reflected shock and pinch phases of the new anode for S65, S67 and S68 (all at 8.0 Torr).
	167
5.34	All possible regions of the occurrence of the Ne SXR pulse for all NN type shots for the new anode ( $a' = 1.2$ cm, $z_0 = 7.3$ cm)
	173
5.35	Comparisons of the measured and computed (using fitted model parameters $f_m = 0.0334$ , $f_c = 0.7$ , $f_{mr} = 0.16$ and $f_{cr} = 0.8$ ) Ne SXR yield for the optimized anode ( $a' = 1.2$ cm, $z_0 = 7.3$ cm)
	173
5.36	Comparisons of the plasma focus pinch length of the original and optimized anode at various pressures
	175
APPENDIX	
A-1	X-ray emission spectrum from neon plasma generated in a plasma focus
	181